Characterisation of 3D porous macrostructure of hollow fibre membranes using X-ray tomography—Effects of some spinning process conditions

J. Viguié [a,b], T. Savart [a], P. Duru [b], J.-C. Rouch [a], J.-C. Remigy [a,*]

[a] Université de Toulouse/CNRS, Laboratoire de Génie Chimique UMR 5503, 118 route de Narbonne 31062 Toulouse cedex 9, France
[b] Université de Toulouse/CNRS, Institut de Mécanique des Fluides de Toulouse UMR 5502, 1 Allée du Professeur Camille Soula 31400 Toulouse, France

Keywords:
X-ray tomography
Hollow fibre membranes
Macrovoids

A B S T R A C T

The presence of pores larger than a micron, known as macrovoids, in polymeric membranes is particularly detrimental for membrane structural integrity and mechanical properties. The theoretical modelling and physical understanding of the mechanisms of initiation and growth of the macrovoids, notably in order to determine processing conditions that would allow to make macrovoids-free membranes, have been the subject of a vast literature and are still controversial. However, experimental data on macrovoids, that could help to discriminate between several ideas are scarce and have been essentially obtained using 2D imaging systems. A very large number of observations are then needed to obtain statistically significant results and the limitation to 2D images does not permit to access to an accurate description of the macroporous structure. In this work, an X-ray tomography system was used to image the 3D porous structure of hollow fibre membranes with a spatial resolution of one micron. Image analysis tools have been developed to accurately characterise the macrovoid shapes and spatial distribution on the membrane outer and inner skins as a function of some of the spinning process conditions (concentration of solvent into the bore and air gap length). The main purpose is therefore to quantify effects of some processing conditions on the macroporous structure of a hollow fibre membrane. Also, such an accurate characterisation of the macrovoids spatial distribution and 3D shape, as well as their variations with the process experimental conditions, help to shed light on macrovoids initiation and growth mechanisms.

1. Introduction

Polymeric membranes are widely used in filtration processes. These applications require well-controlled porous structures. Most of the organic membranes are usually obtained by the well-known phase inversion process. This process consists in triggering a separation between a polymer-rich phase, which forms a continuous matrix of material, and a polymer-lean phase which develops into pores. Phase separation can be achieved by wet-casting (a polymer solution is immersed in a non-solvent bath), dry-casting (solvent is evaporated from a polymer solution) or thermal precipitation. The obtained porous structure is highly dependent on both the phase separation kinetics and the thermodynamical equilibrium.

Some process conditions promote the formation of pores larger than a micron also known as macrovoids. They are particularly detrimental for the structure integrity and for the mechanical resistance to the pressures usually applied during filtration. Macrovoids have commonly pear shape but their geometry may be finger-like or spherical. They have been identified in all phase inversion systems, in flat sheet membranes as well as in the hollow fibre configuration. The mechanisms of initiation and growth are still debated [1–14]. In the case of hollow fibre membrane obtained by wet-casting process, the compositions of the casting solution, the coagulation bath as well as the spinning parameters are known to significantly impact on macrovoid occurrence. Indeed, an increase in polymer concentration [15,16] or solution viscosity, an addition of surfactants [17] or inorganic particles [4] into the casting solution, as well as an addition of solvent into the bore liquid solution [15] may deeply decrease the amount of macrovoids. Spinning velocity [16], air gap [18,19] or spinneret geometry may also significantly influence number, shape and location of macrovoids [18].

These observations are essentially based on the analysis of 2D images of membrane cross sections obtained by scanning electron microscopy or transmission electron microscopy. Coupled with image analysis methods, microscopic techniques enable to get accurate pore size distribution, porosity profile or tortuosity in microfiltration membranes [20,21]. However, this requires a very large number of observations to obtain statistically significant

* Corresponding author. Tel.: +33 561557618.
E-mail address: remigy@chimie.ups-tlse.fr (J.-C. Remigy).

results. Moreover, these techniques do not give access to the actual 3D shape of macrovoids and to their spatial distribution. Such data can be provided by 3D imaging methods such as the X-ray microtomography [22,23] or 3D reconstruction applied to a set of 2D images [24]. In addition to the three-dimensionality, the large volume that can be observed using X-ray microtomography (around 1 mm^3) allows obtaining statistically significant data. Using this technique, Remigy et al. [23] characterised qualitatively the macrovoids 3D shape and dimensions.

Besides the obvious interest of getting images of the membrane internal structure for *a posteriori* process optimisation by trials and errors, this kind of data can also supply precious information on the physical phenomena involved in macrovoid initiation and growth leading to a better understanding which could, *a priori*, help to optimise the process.

The precise physical mechanisms at play leading to macrovoids initiation and growth is a long standing and still controversial issue in the field of membrane formation by phase inversion processes.

Most of the theoretical ideas on macrovoids initiation and growth have been developed for wet-casting as it is the most used process to make membranes for water filtration. A distinction is usually made between the mechanisms at the origin of the macrovoids formation (macrovoid initiation) and those involved during their growth.

Macrovoids initiation is often thought to be promoted by an instability occurring at the casting solution–coagulation bath interface, once the membrane is immersed. Several scenarios have been proposed, which differ from one another by the description of the destabilising mechanisms and also of the overall system (for instance, hydrodynamic instability at the interface between two immiscible fluids, with diffusion of a third component through the interface [10,11], or mechanical instability involving the shrinkage stress induced by solvent synaeresis [9]). Even if the macrovoids growth, following the initial destabilization of the interface, is a highly non-linear phenomenon, their spatial distribution should reflect the physics of the underlying initial instability, and thus be related to the most unstable wavelength that can be obtained through a linear stability analysis. Several studies aimed to detect such a critical wavelength through planar membrane image analysis and confronting its value to the prediction of a stability analysis [12,13]. Interestingly, it must be mentioned that the interfacial instability mechanisms have recently been put forward to explain the formation of hollow fibre membrane with a wavy grooved internal skin [14].

The mechanisms at play during macrovoid growth are also debated. Smolders et al. [3] suggested that macrovoids initiate from nucleation of the polymer-lean phase by liquid/liquid demixing when the composition is located between the binodal and spinodal boundaries on the phase diagram (note that this mechanism does not require an instability of the type mentioned earlier to be triggered). The growth of macrovoids then occurs by diffusion of solvent from the polymer solution to the macrovoid nuclei, when this flow is higher than the non-solvent flow from the nuclei to the polymer solution. However, according to several authors, macrovoid growth cannot be purely diffusive on account of their explosive growth, particularly in dry-casting process [5,6]. McKelvey and Koros [5] suggested that the demixing front velocity governs the macrovoid growth, generating osmotic pressure across the nucleus wall. The arrival of the front may lead to a vitrification at the back side and a pressurisation of the front side, which may explain the characteristic teardrop shape of macrovoids. Paulsen et al. [6] proposed that the diffusion mechanism was helped by a Marangoni force generated by surface tension gradients between the trailing edge and the leading edge of the nascent macrovoid, known as solutocapillary convection. This mechanism was widely accepted [7] and corroborated by experiments using video-microscopy flow-visualisation technique [8]. This technique also enabled the detection of coalescence of micro-droplets with the emerging macrovoids, which is considered by some authors as the predominant phenomenon of the macrovoid growth [23]. Obviously, the final shapes of the macrovoids that can be accurately measured on 3D images are going to reflect the physics involved during their growth.

In this paper, the aim is to characterise quantitatively the 3D distribution of macrovoids as well as their 3D shape and dimensions using X-ray tomography and image analysis techniques. The final purpose is to quantify effects of some processing conditions on the macroporous structure of a hollow fibre membrane. As seen above, such an accurate characterisation of the macrovoids spatial distribution and 3D shape, as well as their variations with the process experimental conditions may help to support one or other of the theoretical mechanisms for macrovoid initiation and growth. This study is organised as follows. The technical aspects related to the processing conditions of the tested hollow fibre membranes, as well as to the X-ray tomography set-up are first presented in Section 2. Then 3D images are exhibited. Methods of detection and characterisation of spatial distribution and 3D shape of macrovoids are then detailed. Results are presented in Section 3: the effect of solvent addition into the bore liquid solution and the influence of the air gap distance are investigated. In the last section, the observed effects are discussed based on the existing theories of macrovoids initiation and growth.

2. Material and methods

2.1. Hollow fibre membrane and process conditions

The hollow fibre membranes were prepared using a dope solution of polyvinylidene fluoride (PVDF) and N-Methyl-2-pyrrolidone (NMP) as solvent. Water was used as coagulant. The nascent hollow fibre extruded from the tip of the spinneret (with an outer diameter of 1.2 mm, a wall thickness of 0.1 mm and an inner diameter of 0.3 mm) and passed into an air gap zone before entering into the a first coagulation bath. The take up speed was set to 11 m min^{-1}. After their elaboration, the hollow fibre membranes were stored into a second water bath to end coagulation for 24 h. Casting solution and bore fluid temperatures were 80 °C while the temperature of the first coagulation bath was 50 °C.

Two sets of membranes were prepared. The first set was made up with an air gap length of 10 cm and three different amounts of solvent added into the bore fluid. The weight percentages of NMP added were 0 wt%, 15 wt% and 30 wt%. The second set was made up with 30 wt% solvent into the bore and six different air gap lengths of 1, 10, 18, 25, 32 and 50 cm, equivalent to residence times in the air of 0.055, 0.55, 0.98, 1.37, 1.75 and 2.7 s respectively. The prepared hollow fibre membranes were washed using RO water and dried gently at room temperature before their characterisation.

2.2. 3D image acquisition by X-ray microtomography

X-ray tomography was performed using the nanofocus computed tomography system NANOTOM® (GE Phoenix, Germany) exhibited in Fig. 1(a). The observed hollow fibre membranes were cylinders of 5 mm in length and around 0.8 mm in diameter, held vertically inserting one end in a glass tube (see Fig. 1(a)). During data acquisition an X-ray beam irradiated the sample. Radiographs of the X-ray beam passing through the sample were

recorded for 2400 different angular positions around the fibre. The complete acquisition time is in hour range under uncontrolled moisture due to the equipment limitation. This is why we observed dry hollow fibres to avoid deformations due to drying during the image acquisition while SRμCT allows the observation of wet fibre [22,23].

A voxel size of around 1 μm^3 was reached. A filtered back projection algorithm (GE Phoenix, Germany) was applied to reconstruct the 3D structure of the sample using scanned radiographs. The reconstructed 3D volume of $900 \times 900 \times 300$ voxels or $900 \times 900 \times 300\ \mu m^3$ represents a 3D map of the absorption coefficients coded in 16 bits. Fig. 1(b) reveals a 2D image in grey levels of a plane perpendicular to the fibre axis, extracted from the 3D volume. One can appreciate on this 2D image the weak contrast between the polymeric matrix and air.

In order to obtain quantitative descriptors of the sample structure, the 3D image was filtered using a median filter (see Fig. 1(c)) and segmented to distinguish porous and solid phases using the AMIRA® software, (see Fig. 1(d)). White pixels represent the solid phase and black pixels the void phase. Fig. 1(e) exhibits a volume extracted from the segmented 3D image. It can be noticed that, due to the spatial resolution, only pores higher than 1 μm^3 (i.e. the voxel size) can be distinguished. Macroporosity can be quantified as the ratio of the number of black pixels within the membrane thickness to the number of white pixels, see Fig. 1(d). Note that the image processing operation leading to a segmented image can induce some uncertainties as far as macroporosity and pore numbers values are concerned, depending on the values of various numerical criteria chosen when running AMIRA® software region-growth algorithm (namely the positions of the "seeding points" and an homogeneity factor for the grey-levels of neighbouring voxels). By tuning these parameters of the region-growth algorithm, the macroporosity was found to vary as much as 4% only, which provides a good estimate of the uncertainty in the macroporosity determination, whereas the number of macropores did not vary significantly.

In the following, a distinction is made between macroporosity near the inner or outer skin. Macroporosity near the outer skin, respectively inner skin, is simply defined as the ratio of the number of black pixels within the outer half, respectively inner half, of the membrane to the number of white pixels within the corresponding half membrane.

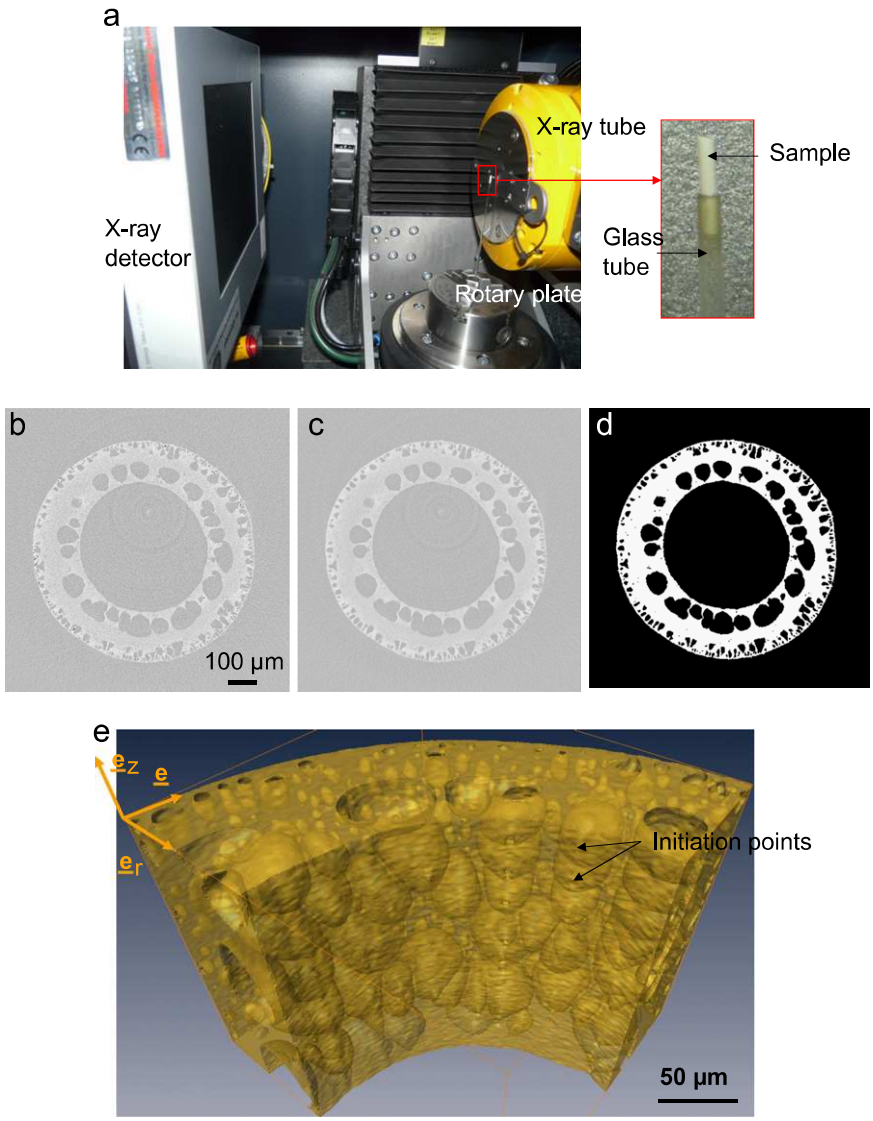

Fig. 1. (a) X-ray tomography set-up (nanofocus computed tomography system NANOTOM® (GE Phoenix, Germany)). (b) 2D image (900×900 pixels) extracted from the imaged volume ($900 \times 900 \times 300$ voxels i.e. $900 \times 900 \times 300\ \mu m^3$). (c) Same image after a filtering operation. (d) Same image after a segmenting operation by region growth. (e) Volume extracted from the 3D segmented image performed with AMIRA® software. The cylindrical coordinate system related to the hollow fibre is noted ($\underline{\mathbf{e}}_r$, $\underline{\mathbf{e}}_\theta$, $\underline{\mathbf{e}}_z$). This image is also available as a supplementary file to the present paper.

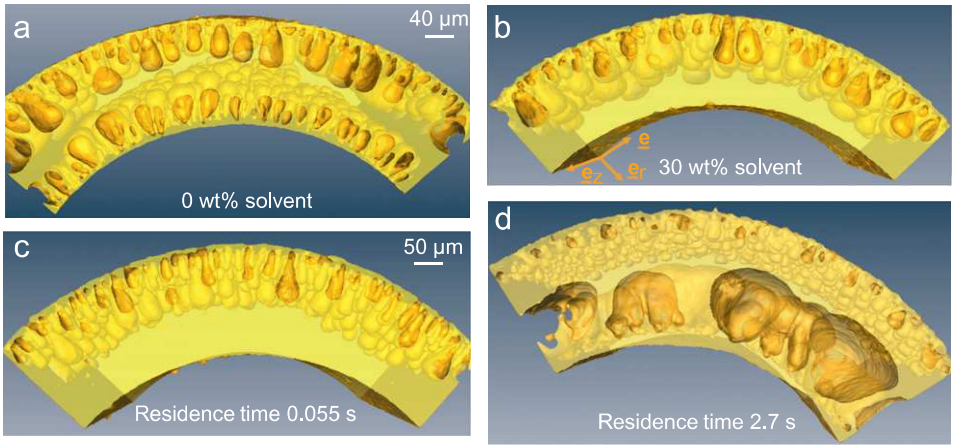

Fig. 2. Volumes extracted from 3D segmented images of hollow fibre membranes made up with (a) 0 wt% and (b) 30 wt% of solvent into the bore liquid solution for a residence time in air of 0.55 s, and with a residence time in air of (c) 0.055 s and (d) 2.7 s with 30 wt% of solvent into the bore liquid. This image is also available as a supplementary file to the present paper.

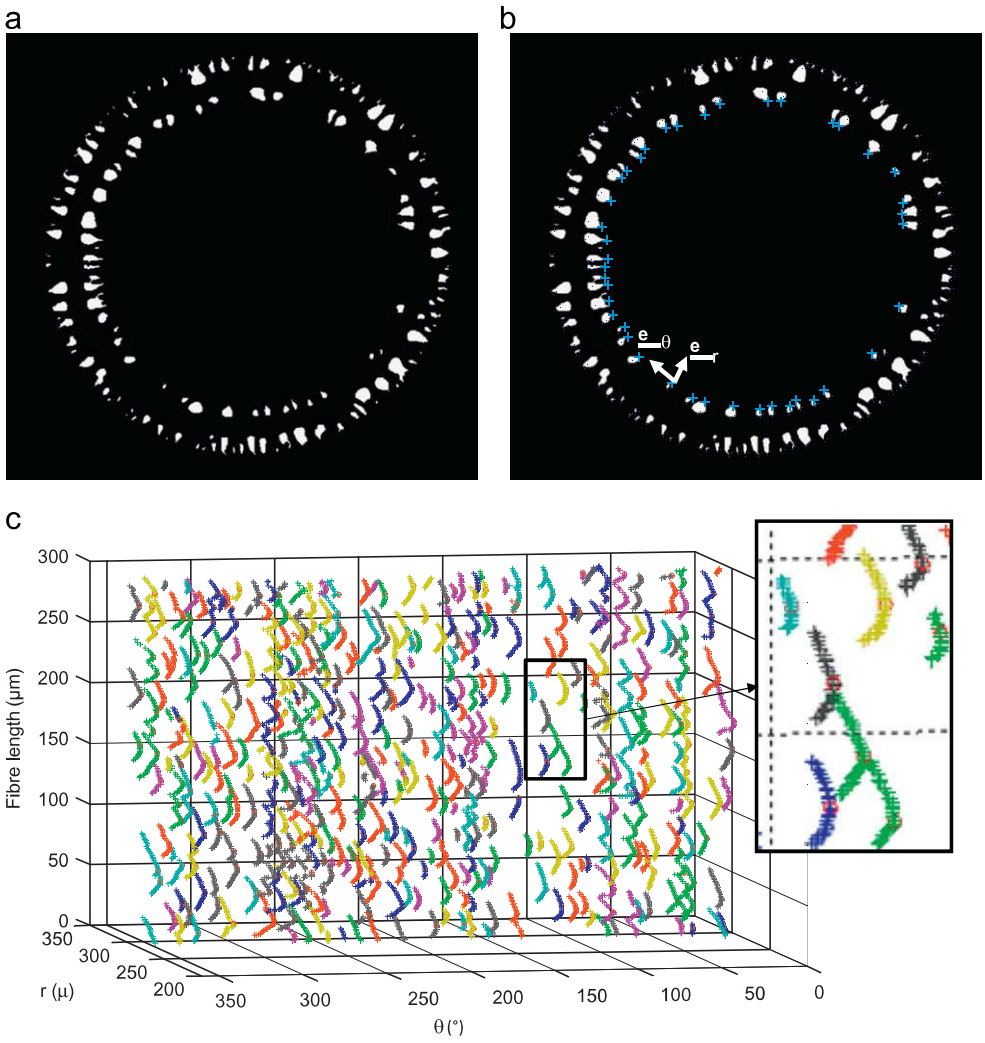

Fig. 3. (a) Porous inclusions in a plane perpendicular to the fibre axis. (b) Inclusions near the inner skin with the nearest points from the fibre centre noted in blue. (c) Representation using the cylindrical coordinate system of these points for the set of 2D images. The local minima are noted by a red circle and correspond to the coordinates of initiation points. (For interpretation of the references to color in this figure legend, the reader is referred to the web version of this article.)

As shown in Fig. 1(e), several macrovoids are connected to each other and appear to be lined up along the $\underline{\mathbf{e}}_z$ direction in some regions. Some of them are also connected to the membrane outside through their initiation points. Fig. 2 presents the top view of the same kind of volumes of hollow fibre membranes obtained with different spinning conditions. Fig. 2(a) and (b)

reveals membrane volumes made up without and with 30 wt% of solvent into the bore liquid solution, respectively. Fig. 2(c) and (d) shows membrane volumes at the lowest and the highest residence time in air respectively (with 30 wt% of solvent into the bore). Differences in macrovoids distributions and shapes between the membrane inner/outer skins and for different process conditions are clearly seen and will be discussed in details in the following, see § 3. Macrovoids with very different sizes can be observed. However, almost all of them appear to have a more or less elongated teardrop (or pear) shape. Widjojo and Chung [18] have also identified similar types of macrovoids using SEM images. The distinction they made between a teardrop shape and a spherical shape (not observed in the present study) may be an artifact due to the 2D visualisation used in their study. In fact, a 3D teardrop shape macrovoid can rather display an elliptical/spherical cross-section, depending on the 2D slice location.

The tools used in this study order to accurately quantify the spatial distribution of the macrovoids on the inner and outer skins of the membrane and their shape, from the 3D images, as a function of some process conditions, are presented in the following.

2.3. Initiation points detection by image analysis

The method to detect initiation points consists of using the set of 2D images perpendicular to the fibre axis. In each image, inclusions belonging to the porous phase are individualised. Fig. 3(a) depicts these inclusions for one 2D image. To detect the initiation points of macrovoids on the inner skin, the nearest point from the fibre centre is found in each inclusion using the "Image processing Toolbox" of MATLAB®. These points are noted in blue in Fig. 3(b). Thereafter, they are plotted for all 2D images in a graph using the cylindrical coordinate system ($\underline{\mathbf{e}}_r$, $\underline{\mathbf{e}}_\theta$, $\underline{\mathbf{e}}_z$) presented in Fig. 1(c), as seen in Fig. 3(c). The points that belong to connected inclusions are grouped and marked with a same local colour. Here, an inclusion in the 'k' image is considered to be connected with another inclusion in the 'k+1' image if the 2D coordinates of the gravity centre of the inclusion in the 'k' image corresponds to a location included in the inclusion of the 'k+1' image. As shown in Fig. 3(c), the local minimum in each set of grouped points is identified and defined as the macrovoid initiation point (noted with a red circle).

Note that the same procedure was applied to detect the initiation points of macrovoids on the outer skin by finding the farthest points from the fibre centre of 2D inclusions of the outer skin. Algorithms were implemented in MATLAB®.

2.4. Characterisation of initiation points spatial distribution

Fig. 4(a) displays an example of the initiation point distribution on the outer skin of a hollow fibre membrane. Here, the perimeter (μm) is used instead of θ. In order to characterise this distribution, the radial distribution function (r.d.f), $g(h)$, was computed. The r.d.f. $g(h)$ represents the probability to find an initiation point in a ring with a width of dh, at a distance h from another initiation point chosen as a reference point. By dividing the physical surface into rings with a width of dh (see Fig. 4(b)) it is possible to compute the number of initiation points $dn(h)$ at a distance between h and $h+dh$ from a given initiation point and to write:

$$g(h) = \frac{S}{N}\frac{dn(h)}{2\pi\, h\, dh} \tag{1}$$

where N represents the total number of initiation points and S the skin area. In order to have a statistically significant measurement of $g(h)$, the r.d.f. was computed for all the initiation points detected and then averaged. Note that to avoid any finite size effects, initiation points that were not positioned sufficiently far away from any of the field of view borders were not taken into account during the average value calculation. Fig. 4(c) exhibits the

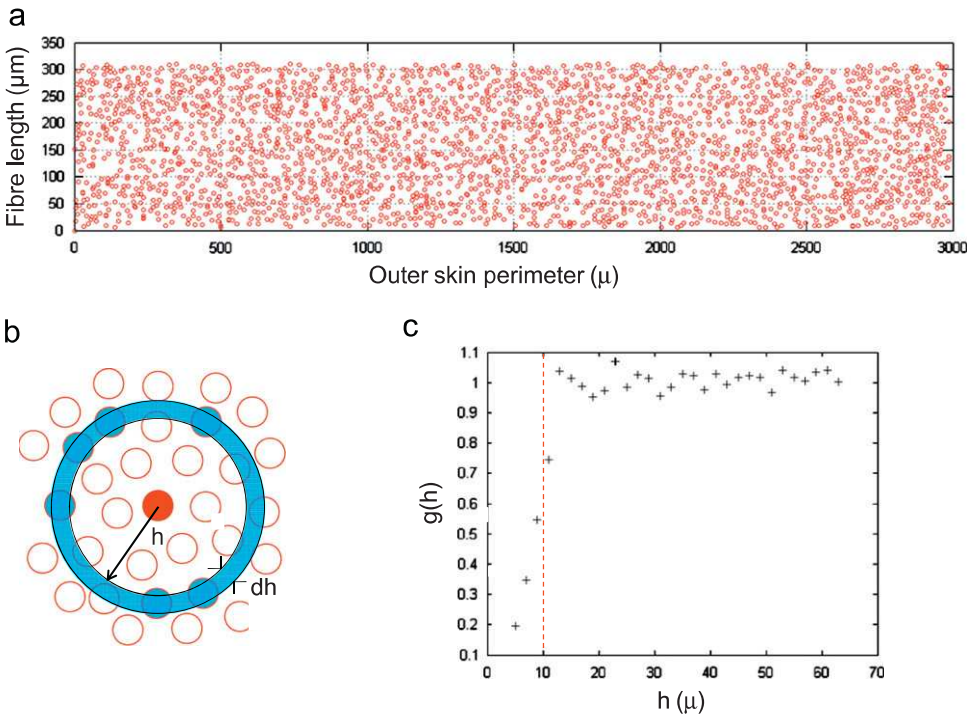

Fig. 4. (a) Example of spatial distribution of the initiation points on the outer skin of a hollow fibre membrane made up without solvent into the bore liquid solution. (b) Scheme of the surface discretisation for the evaluation of the radial distribution function (r.d.f.). (c) Radial Distribution Function (r.d.f.) applied to the distribution of initiation points: evolution of the density $g(h)$ as a function of the distance h from an initiation point. The minimum characteristic length h_{min} detected is around 13 μm (red dashed line). (For interpretation of the references to color in this figure legend, the reader is referred to the web version of this article.)

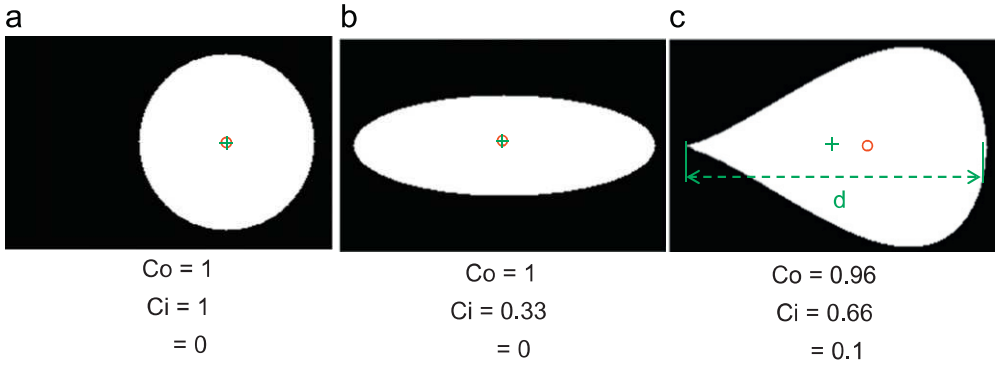

Fig. 5. (a) Circular shape, (b) elliptical shape and (c) teardrop shape with values of concavity *Co*, circularity *Ci* and teardrop shape index λ (distance between the midpoint (green crosses) of the major axis length and the gravity centre (red circles) over the major axis length *d*). (For interpretation of the references to color in this figure legend, the reader is referred to the web version of this article.)

Table 1
Shape indexes for macrovoids of a hollow fibre membrane made up without addition of solvent into the bore (cf. §2.1 and Fig. 2(a)): convexity (*Co*), circularity (*Ci*), teardrop shape index (λ) and relative length (*L*). The shape indexes values are obtained by averaging over all the macrovoids detected on the image. The standard deviation of these average values can be considered as the incertitude on the measurements, and are given in parenthesis.

	Co	*Ci*	λ	*L*
Inner skin	0.85 (0.08)	0.47 (0.14)	0.10 (0.04)	0.27 (0.08)
Outer skin	0.82 (0.11)	0.44 (0.17)	0.07 (0.04)	0.23 (0.12)

evolution of $g(h)$ as a function of h for the initiation points distribution shown in Fig. 4(a). The r.d.f. $g(h)$ reaches a value fluctuating around 1 as soon as $h > h_{min}$ with $h_{min} \approx 13$ µm. This shows that the initiation point distribution is homogeneous beyond this distance. Also, the absence of discernible periodic variations of $g(h)$ around 1 shows that this distribution is random.

2.5. Characterisation of macrovoid shape and dimensions

In order to characterise the various shapes of the macrovoids, and to allow a quantitative and unambiguous study of their evolution as a function of some processing conditions, several shape indexes have been used. Fig. 5(a, b and c) shows respectively a circular, an elliptic and a pear shape with the corresponding shape indexes used in the present study and defined below.

The first index is the convexity, noted *Co*, which is the ratio of the form area over the area into the convex hull. As revealed in Fig. 5, the three shapes are convex. The second index is the circularity, noted *Ci*, which is the ratio of the minor axis length over the major axis length when a shape is fitted by an ellipse. It enables to distinguish an elongated convex shape from a circular convex shape. The ellipse shape and the teardrop shape have circularities lower than 1, attesting that they are elongated forms. The third index is the ratio of the distance between the midpoint of the major axis length (d) and the gravity centre of the shape over the major axis length (d). The midpoint and the gravity centre are plotted as green crosses and red circles respectively in the shapes of Fig. 5. As this index is non-zero for a teardrop shape (see Fig. 5(c)), it enables to distinguish an elliptical shape from a teardrop shape. Thus it is named the teardrop shape index and is noted λ.

The relative macrovoids dimensions have been characterised using the ratio of the major axis length (d) over the thickness of the membrane wall. This index, named relative length, is noted *L*. In order to characterise macrovoids shapes, shape indexes are calculated on each 2D inclusion which contains an initiation point.

The shape indexes defined above have been calculated for the hollow fibre membrane made without addition of solvent into the bore (see Fig. 2(a)) and are given in Table 1 for macrovoids of the inner and outer skins. It is seen that macrovoids have elongated pear shape and their lengths represent around 25% of the whole wall thickness of this hollow fibre membrane. This corresponds quite well to what can be observed with an unaided eye in Fig. 2(a), which shows the relevance of these indexes to characterise the macrovoids shape. Note that the wall thickness in this case is around 130 µm; thereby macrovoids have an average length of 32 µm.

3. Results

3.1. Influence of solvent addition into the bore fluid

3.1.1. On macroporosity and spatial distribution of initiations points

Fig. 6(a) depicts the evolution of the macroporosity near the inner skin, near the outer skin and for the whole membrane when the solvent ratio into the bore liquid solution varies from 0 to 30 wt%. Fig. 6(b) exhibits the evolution of the surface density of initiation points on the inner skin and on the outer skin for the same variations of solvent content.

It appears that the whole macroporosity decreases regularly. The macroporosity close to the inner skin drops from 0.3 to almost 0. Quite surprisingly, the macroporosity close to the outer skin is also affected, varying from 0.42 to 0.35 with the addition of solvent. The outer skin properties (permeability and selectivity) are thus probably also affected by a change of the bore fluid composition. To our knowledge, this is the first time that this observation is reported.

The density of initiation points is almost three times higher on the outer skin than on the inner skin without solvent addition. It can be noticed that the density of initiation points (i.e. macrovoids) is one thousand times lower than the density of pores (smaller than a micron) commonly measured for that kind of membranes (around 10^{12} m^{-2}) [25]. The evolution of the initiation point density on the outer skin almost follows the same evolution as macroporosity. However, the macroporosity near the inner skin shows a 15% decrease while the density of initiation points on the inner skin is divided by 4 as the solvent ratio varies from 0 to 15 wt%: the macrovoids are then larger and fewer when the solvent ratio increases from 0 to 15 wt% before almost disappearing with a further increase of the solvent concentration up to 30 wt%.

The distribution of initiation points on the outer skin was found to be homogeneous and random whatever the solvent

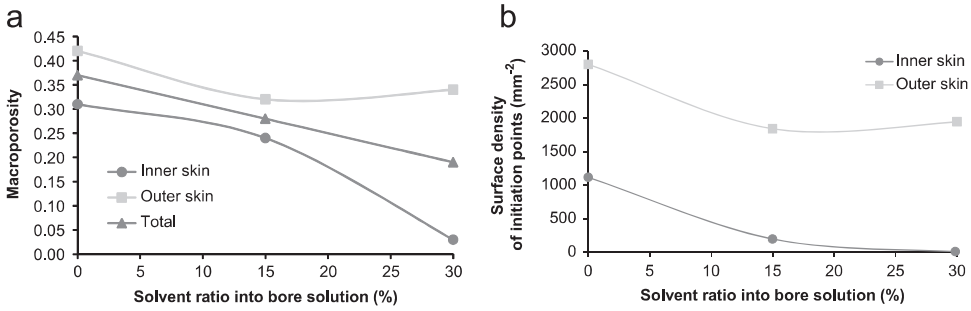

Fig. 6. (a) Effect of solvent addition (wt%) into the bore on the macroporosity close to the inner skin, close to the outer skin and for the whole membrane. As mentioned in §2.b, a maximum uncertainty of 4% on the macroporosity values can be induced, depending on the way the image segmentation is performed. This uncertainty would affect all the data points similarly, shifting all of them to values slightly larger or smaller than those presented in this figure. (b) Effect of solvent addition (wt%) into the bore fluid on the surface density of macrovoids on the inner skin and on the outer skin.

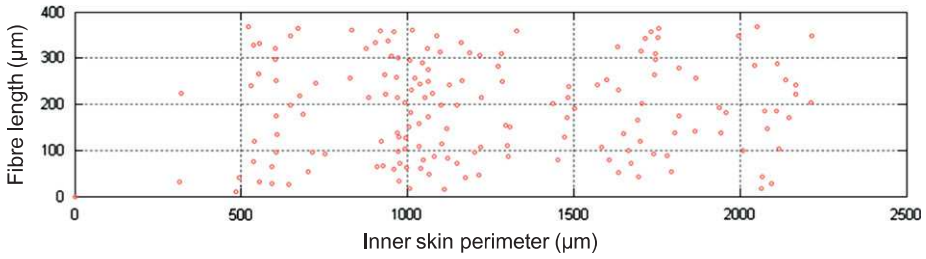

Fig. 7. Spatial distribution of the initiation points on the inner skin of a hollow fibre membrane made up with 15 wt% of solvent into the bore fluid.

Table 2
Effect of solvent addition into the bore on the minimum characteristic length h_{min} between initiation points on the inner and outer skins.

h_{min} (µm)	0 wt%	15 wt%	30 wt%
Inner skin	20	–	–
Outer skin	13	17.5	16.5

content into the bore fluid is. For each membrane, a minimum characteristic length can be measured. However, the distributions of the initiation points on the inner skin are largely heterogeneous when solvent is added to the bore (i.e. for 15 wt% and 30 wt%). Fig. 7 shows this distribution for a 15 wt% solvent ratio. Because of the heterogeneity of the distribution, no accurate minimum characteristic length could be measured using the radial distribution function on the inner skin, neither for solvent ratio of 15 wt%, nor for one of 30 wt%.

However, in these cases, initiation points appear to be grouped in some regions and sometimes lined up along the fibre length direction $\underline{\mathbf{e}}_z$. No alignment cannot be distinguished in the outer skin (see Fig. 4(a)) and in the inner skin for 0 wt% solvent into the bore. The minimum characteristic lengths between initiation points h_{min} for the different solvent ratios are given in Table 2.

As expected, h_{min} is much smaller at 0 wt%, when the density of initiation points is large, than at the two solvent concentrations used for which the density of initiation points significantly decreases. It is larger for initiation points on the inner skin (at 0 wt% of solvent into the bore), reaching 20 µm.

3.1.2. *On macrovoid shape and dimensions*

The convexity (Co) and the teardrop shape index (λ) are almost always higher than 0.8 and 0.08, respectively. This attests that macrovoids have nearly a teardrop shape. Fig. 8(a), and (b), presents the evolution of the mean circularity of the 2D inclusions, respectively of their mean relative length, with the solvent addition. No variation can be observed for both indexes for macrovoids close to the outer skin. However, the circularity of macrovoids close to the inner skin sharply increases from 0.44 to 0.80 when the solvent ratio varies from 0 to 30 wt%. However, no variation is noticed on the macrovoids relative length. We can observe that the relative length is almost similar, around 22%, whatever the location (inner skin or outer skin) and the solvent ratios are. Nevertheless, as the membrane thickness slightly decreases with solvent addition from 140 µm to 130 µm, the actual mean macrovoid length is reduced from 30 µm to 28 µm. The mean width of macrovoids near the outer skin remains around 13 µm whereas it increases from 14 µm to 24 µm for macrovoids near the inner skin when the solvent ratio varies from 0 to 30 wt%.

It can be concluded that macrovoids close to the inner skin are getting wider with the increase of solvent ratio into the bore fluid as illustrated in Fig. 9. As seen previously, see Fig. 6(a and b), the number of macrovoids decreases while increasing the solvent concentration. From 0 to 15 wt%, the macrovoid volume increase explains the small reduction of the macroporosity near the inner skin. At 30 wt%, the macrovoids are still wider but they are very few which explains the sharp decrease of the macroporosity.

3.2. *Influence of residence time in the air (i.e. air gap length)*

3.2.1. *On macroporosity and spatial distribution of initiation points*

Fig. 10(a) depicts the evolution of the macroporosity close to the inner skin, close to the outer skin and for the whole membrane when the residence time in air varies from 0.1 s to 2.7 s (i.e. a variation of the air gap from 1 cm to 50 cm, cf. §2.a.). Fig. 10(b) exhibits the evolution of the surface density of initiation points on the inner skin and on the outer skin for the same variation of residence time. It appears that macroporosity of the whole membrane slightly increases. This evolution can be ascribed to the great increase of the macroporosity close to the inner skin from 0.08 for the minimum tested residence time (0.055 s) to 0.6 for the maximum tested residence time (2.7 s).

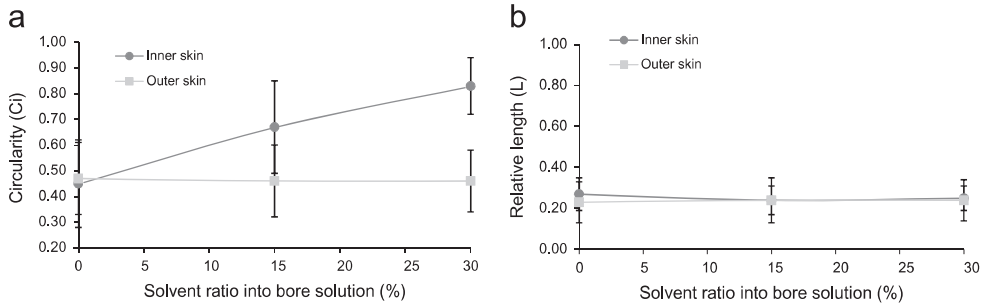

Fig. 8. (a) Effect of solvent addition (wt%) into the bore liquid solution on the circularity *Ci* of macrovoid shapes. (b) Effect of solvent addition (wt%) into the bore fluid on the relative length *L* of macrovoid. The error bars shown correspond to the standard deviation of the mean value, averaged over all the macrovoids detected on the given image.

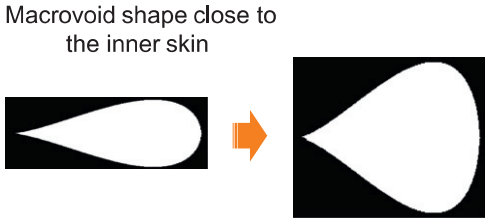

Fig. 9. Qualitative evolution of the shape and dimensions of macrovoids located near the inner skin when the solvent ratio into the bore varies from 0 wt% to 30 wt%.

A sharp increase is noticed between 1 s and 1.4 s which is related to a sudden increase of initiation points density on the inner skin. As shown in Fig. 10(b), the density of initiation points is close to zero for residence times lower than 1.4 s and around 400 mm^{-2} beyond. This particular residence time can be considered as a critical time for macrovoid formation. Besides, it is worth noting that macroporosity significantly increases whereas the density of initiation points does not change.

Macroporosity near the outer skin and density of initiation points on the outer skin show variations as the residence time increases but no clear trend emerges. These results slightly differ from the SEM observations of Widjojo and Chung [18] who noticed an increase in the number of macrovoids near the inner skin and a decrease in the number of macrovoids near the outer skin with increasing air gaps.

The initiation point distribution on the outer skin was found to be homogeneous and random whatever the residence time is. No significant variation of the minimum characteristic length has been recorded while varying the residence time. This value is around 17 µm. Distributions of initiation points on the inner skin are heterogeneous. As for the distribution on the inner skin of membrane made with solvent into the bore solution, we can distinguish some initiation points lined up along the fibre length direction. Regarding the initiation points distributions and their surface densities, it appears that distributions are heterogeneous when their densities are lower than 500 mm^{-2}. In this case, we can distinguish that initiation points tend to line up along the fibre length direction. These results corroborate quite well those obtained with the solvent ratio change (cf. §3.a.i.).

3.2.2. *On macrovoid shape and dimensions*

Fig. 11(a) presents the evolution of the mean circularity of the 2D inclusions which have initiation points with the residence time in the air. Fig. 11(b) exposes the evolution of the mean relative length. The circularity of macrovoids near the inner skin remains around 0.7 when the residence time increases while the relative length doubles between the minimum and the maximum tested residence times. The circularity of macrovoids near the outer skin increases regularly with the residence time while the relative length decreases. Note that the mean circularity and the mean relative length of macrovoids close to the outer skin are lower than those of macrovoids close to the inner skin whatever the residence time is.

One can conclude that macrovoids are always larger near the inner skin than near the outer skin. When the residence time increases, the membrane thickness increases too from 125 µm to 150 µm and macrovoids near the inner skin become larger as it is represented in Fig. 12(a): their mean length and their mean width increase from 40 µm to 90 µm and from 30 µm to 60 µm, respectively. The macrovoids close to the outer skin are shorter: their actual mean length is reduced from 30 µm to 18 µm. On the contrary, their mean width does not significantly evolve and remains around 9–10 µm (the increase of their circularity is compensated for by the increase of membrane thickness). This is represented in Fig. 12(b).

4. Discussion

4.1. *Contribution to the understanding of macrovoid initiation mechanisms*

The analysis of the spatial distribution of the macrovoids initiation points near the inner and outer skins provides some information about the mechanisms governing macrovoids initiation. The present results suggest that the spatial distributions are directly related to the densities of initiations points on both skins. When the density is lower than 500 mm^{-2}, distributions appear to be heterogeneous and the r.d.f. is not an appropriate tool to characterise them. However, it can be clearly seen that, in this case, macrovoids tend to line up along the fibre axial direction. When the density is equal or greater than 1000 mm^{-2}, distributions appear to become quite homogeneous and random on both skins: initiation points alignments cannot be distinguished anymore. In this case, a minimum characteristic length between initiation points can be measured. As expected, it decreases as the density increases. This characteristic length is significantly larger than the macrovoids mean width when the density is equal or lower than 2000 mm^{-2} indicating that there is no contact between macrovoids. Beyond this density, the characteristic length is similar to the macrovoid width indicating that macrovoids begin to be connected one to another. In particular, it is the case for macrovoids near the outer skin of membranes made without solvent into the bore (cf. §3.a.).

A characteristic length between macrovoids has already been observed and measured in asymmetric 2D flat sheet membranes by Cohen-Addad and Panine [13]. They obtained experimentally

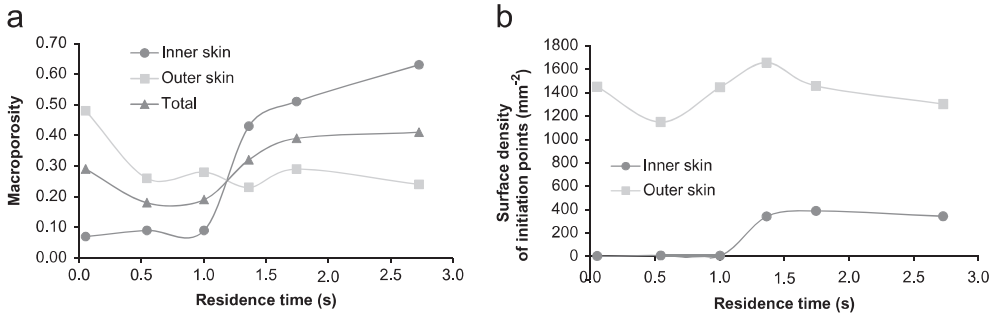

Fig. 10. (a) Effect of residence time in the air on the macroporosity close to the inner skin, close to the outer skin and for the whole membrane. (b) Effect of residence time in the air on the surface density of macrovoids on the inner skin and on the outer skin.

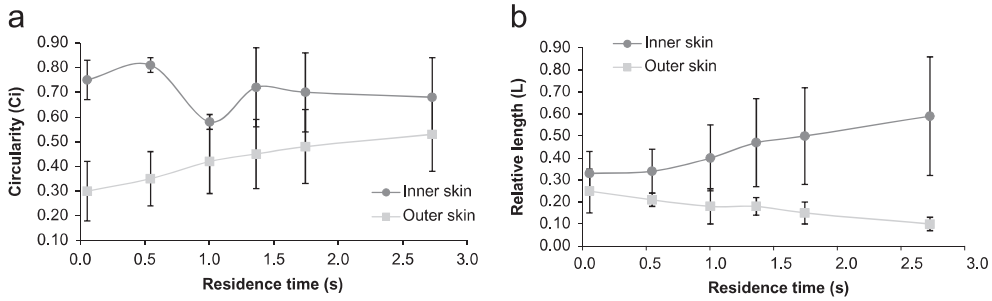

Fig. 11. (a) Effect of residence time in air on the circularity of macrovoid shapes. (b) Effect of residence time in air on the relative length L of macrovoids.

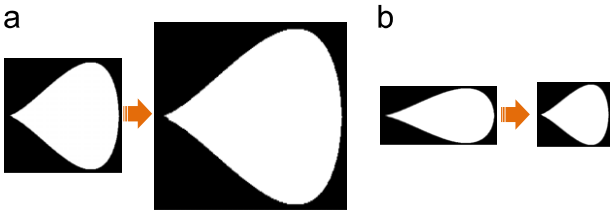

Fig. 12. Qualitative evolution of the shape and dimensions of macrovoids when the residence time in the air varies from 0.055 s to 2.7 s for macrovoids (a) close to the inner skin and (b) close to the outer skin.

some scaling laws relating this length to the solvent concentration and to the diffusion coefficients near the interface between the casting solution and the non-solvent bath, which made sense within the framework of a qualitative instability analysis. A similar finding, again for flat sheet membranes was obtained by Ray et al. [12]. In the case of hollow fibre membranes, this is to our knowledge the first time that such a characteristic length is measured, which may serve as a reference data to be matched by theoretical predictions related to macrovoids initiation, for instance using the linear stability analysis framework.

The existence of such a characteristic length can also be understood within the framework of Prakash et al. approach [9]. According to these authors, the macrovoid initiation is caused by the rupture of stressed necks of the gelled polymer-rich network. This should result in a region where stresses are relaxed around the broken neck thus giving a characteristic spacing between macrovoids initiation points, which still needs to be quantitatively predicted in the framework of this theory.

The initiation points lining up (at low density) may imply that there is an effect of the fibre motion on macrovoids formation in hollow fibre membranes. Following again Prakash et al., we may think that the mechanical weakness of some necks may propagate, promoted by the fibre motion. The fibre motion effect on the macrovoid initiation appears to be significant as long as the macrovoids density remains low. However, it is worth noting that it is no longer the case at higher density, where the initiation point distribution is homogeneous and random.

4.2. Coherence of the present results with the current knowledge on macrovoids growth mechanisms

As shown in the present work, solvent addition into the bore leads to a reduction of initiation points on the inner skin and to an increase of the macrovoids width. The reduction of initiation points with solvent addition has been already noticed [15]. It is viewed as the result of a delayed demixing which leads to nuclei and then droplets that are too small to coalesce. Indeed, coalescence of droplets is usually thought to be a requirement for macrovoid formation and growth [3,9]. Besides the reduced number of macrovoids finally formed, the measured increase of their width may be the consequence of a delayed vitrification of the polymer-rich phase owing to a slow evacuation of solvent.

Membranes made with different residence times have been obtained using a 30 wt% solvent ratio into the bore. As a result, there are barely any macrovoids close to the inner skin at short residence times. However, macrovoids are significantly more numerous beyond a critical residence time in air (or equivalently a critical air gap) estimated to 1–1.5 s. Before the hollow fibre falls into the bath, phase inversion occurs almost exclusively near the inner skin. As the solvent cannot be expelled, the solvent concentration into the bore fluid increases more and more. Moreover, there is no front of non-solvent migrating from the outer skin. Thus, vitrification cannot occur before the hollow fibre falls into the bath. For short residence times, the formed droplets have not enough time to grow (obviously because of the significant delayed demixing at high solvent ratio into the bore) so as to coalesce before gelification and vitrification of the polymer-rich phase. Beyond the critical time, droplets can grow enough to coalesce and so to form macrovoids.

Then, it can be noticed that the size of macrovoids close to the inner skin tends to increase with the residence time. Indeed, once droplets have coalesced, macrovoids are free to grow before vitrification. As a result, the formed macrovoids are larger and larger as the residence time increases. Besides, denser regions are created in front of the macrovoids. When the nascent membrane enters into the coagulation bath, phase inversion occurs close to the outer skin. The leading edges of the developing macrovoids close to the outer skin are pressurised when meeting the dense regions. Consequently, macrovoids close to the outer skin are shorter in length than those created at short residence times.

5. Conclusions

In this work, the X-ray tomography technique has been used, along with some 3D image analysis tools, in order to accurately characterise the shape and spatial distribution of macrovoids present close to hollow fibre membrane inner and outer skins. These morphological characteristics are a function of the processing parameters, which impact the phase inversion phenomenon leading to the membrane. In this study, the effects of solvent addition into the bore and of the residence time in the air have been investigated.

The present work demonstrates the relevance of X-ray tomography for hollow fibre membrane 3D morphological characterisation. For instance, the 3D nature of the data allows showing unambiguously the existence of a range of processing conditions for which a minimum characteristic distance between macrovoids initiation points can be measured. This observation is in accordance with several theories drawn to account for macrovoids initiation, in particular a recent theory based on mechanical instability of the gelled polymer phase. Besides, the 3D shape characterisation of macrovoids enables to establish relations between their amount and shapes, and between the demixing and vitrification kinetics. However, this point has been only briefly discussed. It appears necessary to study the effects of other spinning conditions on these macrovoids parameters. Also, it could be interesting to perform X-ray tomography imaging during the phase inversion in order to follow the macrovoids growth in situ to observe their formation. Finally, the 3D images could also be used to determine the effective transport properties (e.g. permeability tensor) of the membrane.

Acknowledgements

This work would not have been possible without the financial support of the French Research Federation FERMaT in Toulouse.

References

[1] M.A. Frommer, R.M. Messalem, Mechanism of membrane formation. VI. Convective flows and large void formation during membrane precipitation, Ind. Eng. Chem. Prod. Res. Dev. 12 (1973) 328–333.
[2] H. Strathmann, K. Kock, P. Amar, R.W. Baker, The formation mechanism of asymmetric membranes, Desalination 16 (1975) 179–203.
[3] C.A. Smolders, A.J. Reuvers, R.M. Boom, I.M. Wienk, Microstructures in phase-inversion membranes. Part1. Formation of macrovoids, J. Membr. Sci. 73 (1992) 259–275.
[4] S. Husain, W.J. Koros, Macrovoids in hybrid organic/inorganic hollow fibre membranes, Ind. Eng. Chem. Res. 48 (2009) 2372–2379.
[5] S.A. McKelvey, W.J. Koros, Phase separation, vitrification, and the manifestation of macrovoids in polymeric asymmetric membranes, J. Membr. Sci. 112 (1996) 29–39.
[6] F.G. Paulsen, S.S. Shojaie, W.B. Krantz, Effect of evaporation step on macrovoid formation in wet-cast polymeric membranes, J. Membr. Sci. 91 (1994) 265–282.
[7] M.R. Pekny, A.R. Greenberg, V. Khare, J. Zartman, W.B. Krantz, P. Todd, Macrovoid pore formation in dry-cast cellulose acetate membranes: buoyancy studies, J. Membr. Sci. 205 (2002) 11–21.
[8] M.R. Pekny, J. Zartman, W.B. Krantz, A.R. Greenberg, P. Todd, Flow-visualisation during macrovoid pore formation in dry-cast cellulose acetate membranes, J. Membr. Sci. 211 (2003) 71–90.
[9] S.S. Prakash, L.F. Francis, L.E. Scriven, Microstructure evolution in dry-west cast polysulfone membranes by cryo-SEM: a hypothesis on macrovoid formation, J. Membr. Sci. 313 (2008) 135–157.
[10] C.V. Sternling, L.E. Scriven, Interfacial turbulence: hydrodynamic instability and the Marangoni effect, AIChE J. 5 (1959) 514–523.
[11] T.S. Sørensen, M. Hennenberg, A.J. Sanfeld, Deformational instability of a plane interface with perpendicular linear and exponential concentration gradients, J. Colloid Interface Sci. 61 (1977) 62–76.
[12] R.J. Ray, W.B. Krantz, R.L. Sani, Linear stability theory model for finger formation in asymmetric membranes, J. Membr. Sci. 23 (1985) 155–182.
[13] J.P. Cohen Addad, P. Panine, Pore generation in asymmetric polymeric membranes, Polym. Bull. 42 (1999) 345–352.
[14] J. Yin, N. Coutris, Y. Huand, Role of Marangoni instability in fabrication of axially and internally grooved hollow fibre membranes, Langmuir 26 (22) (2010) 16991–16999.
[15] Y. Liu, G.H. Koops, H. Strathmann, Characterisation of morphology controlled polyethersulfone hollow fibre membranes by the addition of polyethylene glycol to the dope and bore liquid solution, J. Membr. Sci. 223 (2003) 187–199.
[16] N. Peng, T.S. Chung, K.Y. Wang, Macrovoid evolution and critical factors to form macrovoid-free hollow fibre membranes, J. Membr. Sci. 318 (2008) 363–372.
[17] D.M. Wang, F.C. Lin, T.T. Wu, J.Y. Lai, Formation mechanism of the macrovoids induced by surfactant additives, J. Membr. Sci. 142 (1998) 191–204.
[18] N. Widjojo, T.S. Chung, Thickness and air gap dependence of macrovoid evolution in phase-inversion hollow fibre membranes, Ind. Chem. Res. (2006) 7618–7626.
[19] H.A. Tsai, C.Y. Kuo, J.H. Lin, D.M. Wang, A. Deratani, C. Pochat-Bohatier, K.R. Lee, J.Y. Lai, Morphology control of polysulfone hollow fibre membranes via water vapor induced phase separation, J. Membr. Sci. 278 (2006) 390–400.
[20] R. Ziel, A. Haus, A. Tulke, Quantification of the pore size distribution (porosity profiles) in microfiltration membranes by SEM, TEM and computer image analysis, J. Membr. Sci. 323 (2008) 241–246.
[21] C. Torras, D. Puig, M.A. García, A new method to quantify parameters of membrane morphology from electron microscopy micrographs by texture recognition, Chem. Eng. Sci. 66 (2011) 4582–4594.
[22] J.C. Remigy, M. Meireles, Assessment of pore geometry and 3-D architecture of filtration membranes by synchrotron radiation computed microtomography, Desalination 199 (2006) 501–503.
[23] J.C. Remigy, M. Meireles, X. Thibault, Morphological characterisation of a polymeric microfiltration membrane by synchrotron radiation computed microtomography, J. Membr. Sci. 305 (2007) 27–35.
[24] H. Reingruber, A. Zankel, C. Mayrhofer, P. Poelt, Quantitative characterisation of microfiltration membranes by 3D reconstruction, J. Membr. Sci. 372 (2011) 66–74.
[25] A.L. Zydney, L.J. Zeman, Microfiltration and ultrafiltration. Principles and applications, Marcel Dekker, Inc., New York, 1996.